The Astrophysical Journal, 891:88 (8pp), 2020 March 1 https://doi.org/10.3847/1538-4357/ab711b

White-light Emission and Chromospheric Response by an X1.8-class Flare on 2012 October 23

Kyoko Watanabe[1] and Shinsuke Imada[2]
[1] National Defense Academy of Japan, 1-10-20 Hashirimizu, Yokosuka 239-8686, Japan; kwatana@nda.ac.jp
[2] Institute for Space-Earth Environmental Research (ISEE), Nagoya University, Furo-cho, Chikusa-ku, Nagoya 464-8601, Japan
Received 2018 October 18; revised 2020 January 17; accepted 2020 January 27; published 2020 March 6

Abstract

On 2012 October 23, a strong white-light emission, associated with an X1.8-class flare, was observed by the Solar Optical Telescope on board the *Hinode* satellite. White-light kernels were clearly observed along the Ca II H ribbons. *RHESSI* also observed hard X-ray emissions that were almost located on the white-light kernels. The total energy of the white-light emission was $\sim 10^{27-28}$ erg s^{-1} and the total energy of the accelerated electrons was almost of the same order when we used 40 keV as the lower energy cutoff. The white-light emission appears to have originated from nonthermal electrons in these energies. Moreover, the EUV imaging spectrometer on board the *Hinode* satellite performed a raster scan over this flaring active region and the flare occurred during the scan. Over the white-light kernels, we observed redshifts of a few tens of km s^{-1} in Fe XII. It appears that these EUV responses originated from some accelerated electrons due to the solar flare and they are considered to be the source of the white-light emission. In fact, the electron density of the white-light kernels was less than 10^{12} cm^{-3}, which is sufficiently low for nonthermal electrons to penetrate into the photosphere.

Unified Astronomy Thesaurus concepts: Solar chromosphere (1479); Solar white-light flares (1983); Solar ultraviolet emission (1533)

1. Introduction

The origin of energetic particles is a long-standing unresolved problem in the area of astrophysics. Frequent observations indicate that high-energy particles are generated in explosive energy release events such as solar flares and terrestrial substorms. Many theoretical and observational studies have attempted to understand the origin of high-energy particles and various mechanisms have been proposed, such as shock acceleration (e.g., Blandford & Ostriker 1978). Magnetic reconnection is also considered to be a source of energetic particles. For example, in the Earth's magnetosphere, energetic particles are often observed in the vicinity of magnetic reconnection regions (e.g., Sarris et al. 1976; Øieroset et al. 2002; Imada et al. 2007, 2011). Solar flares (e.g., Tsuneta et al. 1992; Imada et al. 2013) are also considered to be associated with magnetic reconnection and they are another important source of particle acceleration. The solar atmosphere is an excellent space laboratory for studying particle acceleration, and many studies have investigated high-energy particles during solar flares in recent decades. Substantial progress has been made in our understanding of particle acceleration in the last three decades, mainly because of modern satellite observations in the hard X-ray region (e.g., Masuda et al. 1994). Furthermore, enhancements have sometimes been observed in the hard X-ray region but also in terms of visible continuum radiation, which is known as a "white-light flare," where this is associated with strong solar flares. Many of these observed events were characterized by strong correlations between the time profiles and locations of white-light emissions, as well as hard X-rays and/or radio emissions (e.g., Hudson et al. 2006; Watanabe et al. 2010a; Krucker et al. 2011; Kuhar et al. 2016), so it seems that the source of white-light emissions is nonthermal electrons. In addition, white-light emission (especially core emission) is generally emitted from near the photosphere (e.g., Watanabe et al. 2012), but nonthermal electrons are almost thermalized by the time they reach the lower chromosphere (Neidig 1989) if we assume a uniform solar atmosphere similar to that in the VAL-C model (Vernazza et al. 1981). Theoretically, only the most highly energetic electrons with energies of more than 900 keV can reach the photosphere (Neidig 1989). Therefore, there is a problem in terms of the emission height difference between white-light and hard X-ray emissions, and how the energy of nonthermal electrons propagates to the photosphere and produces white-light emissions.

Recently, Martínez Oliveros et al. (2012) found that a white-light emission was located at almost the same height as the hard X-ray emission based on observations using the Helioseismic and Magnetic Imager (HMI; Scherrer et al. 2012; Schou et al. 2012) on board the *Solar Dynamics Observatory* (*SDO*; Pesnell et al. 2012) and *RHESSI* (Lin et al. 2002). Thus, observations of this event indicate that accelerated electrons can reach the photosphere. However, they cannot explain how nonthermal electrons might reach the photosphere through the solar atmosphere. Battaglia & Kontar (2012) also estimated the white-light emission height from the same event and obtained the different result of white-light emission originating from the lower chromosphere. This result was explained by the radiative back-warming model of white-light emission.

In general, the plasma condition is totally different during a flare from a quiet Sun in the solar corona but also in the transition region and/or upper chromosphere. Thus, it is possible that the different plasma conditions in the chromosphere/transition region might affect the transport of energetic electrons from the corona to the photosphere. In this study, we aimed to determine the physical plasma condition from the corona to the lower chromosphere above the white-light kernels. Furthermore, we attempted to predict how white-light emissions can be produced by the transportation of nonthermal electrons in a white-light flare.

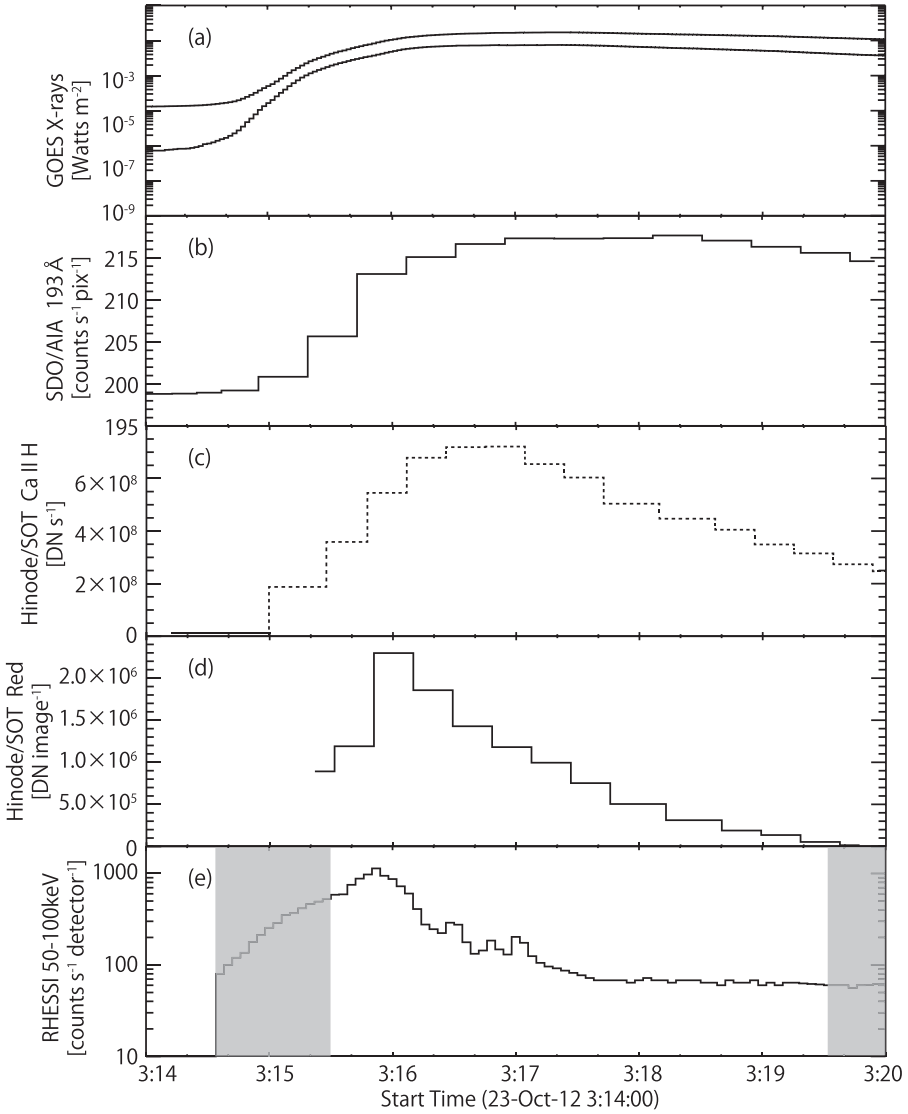

Figure 1. (a) Light curves obtained for soft X-rays observed by *GOES*, (b) 193 Å UV emission by *SDO*/AIA, (c) Ca II H, and (d) white-light (red continuum) emission by *Hinode*/SOT, and (e) hard X-ray corrected count rate by *RHESSI*. Gray regions have pile-up issues. We did not use saturated images for the 193 Å light curve. The Ca II H emission was estimated from Ca II H images by collecting pixel data numbers over 1500 from the flare mode data. Ca II H emissions were saturated in the image after 03:15 UT, as shown in Figure 2, and the Ca light curve was not correct after that time (dotted line). White-light emission was estimated from difference images, and the subtracted reference image for the difference was taken at 03:20:06 UT, which was immediately after the end of the white-light enhancements. No hard X-ray data were available before 03:14:34 UT because the *RHESSI* was in the South Atlantic Anomaly (SAA).

2. Emission Timings of an X1.8-class Flare

On 2012 October 23, an X1.8-class flare occurred in the active region of NOAA 11598, which was located at S 13° E 58°. This flare started at 03:13 UT, where the soft X-ray flux peaked at 03:17 UT and ended at 03:21 UT, and thus this was a highly compact event with a duration of less than 10 minutes. Figure 1(a) shows the *Geostationary Operational Environmental Satellite* (*GOES*) soft X-ray profile. Almost the same behavior was observed in the light curve of the 193 Å UV emission detected by the Atmospheric Imaging Assembly (AIA; Lemen et al. 2012) on board the *SDO*, as shown in Figure 1(b). The AIA captures an image every 12 s but we did not use saturated images for this light curve because of their exposure time.

All three *Hinode* instruments also successfully observed this flare. The X-Ray Telescope (XRT; Golub et al. 2007) automatically detected this flare at 03:15 UT due to a sudden increase in the X-ray flux in its field of view (FOV) and it shifted to the flare observation mode (Kano et al. 2008). The Solar Optical Telescope (SOT) (Ichimoto et al. 2008; Shimizu et al. 2008; Suematsu et al. 2008; Tsuneta et al. 2008) also shifted to the flare observation mode due to the XRT flare trigger. In the flare observation mode, the SOT uses a FOV of at least 108.″5 × 108.″5 with an effective spatial resolution (2 × 2 summing) of 0.″108 pixel^{-1}, and it captures images in at least the Ca II H (3968.5 Å, width 3 Å), red (6684.0 Å, width 4 Å), green (5550.5 Å, width 4 Å), and blue (4504.5 Å, width 4 Å) filters every 20 s, where the exposure times for each wavelength are 123 ms, 51 ms, 77 ms, and 61 ms, respectively.

One Ca II H image was observed before starting the flare observation mode, as shown in the top left panel in Figure 2. This image was captured during the beginning of the impulsive phase. The Ca II H ribbons started to form at this time and any Ca II H emissions were not saturated yet. In addition, although clear Ca II H ribbons were seen in the flare observation mode, most of

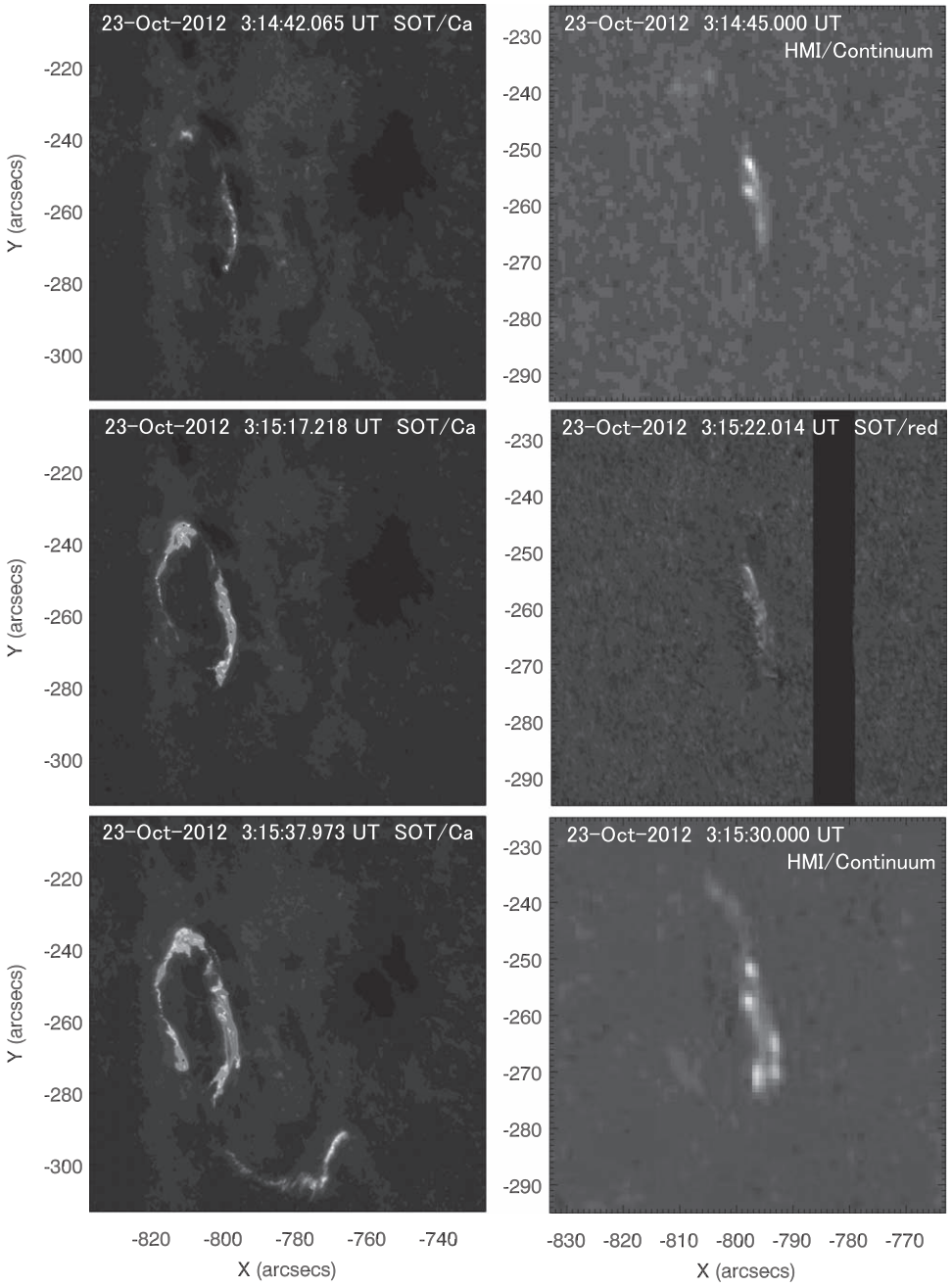

Figure 2. Left: Ca II H images observed by *Hinode*/SOT. The top image was captured at the time of flare onset and immediately before the start of flare mode observations (at an effective spatial resolution of 0.″218 pixel^{-1} and an exposure time of 150 ms). The images at the center and bottom were obtained from flare mode observations (at an effective spatial resolution of 0.″108 pixel^{-1}, with image capture every 20 s, and an exposure time of 123 ms). All of the Ca II H images were saturated during the flare mode observations. Top and bottom right: running difference images of the continuum band observed by the *SDO*/HMI (at an effective spatial resolution of 0.″6 pixel^{-1} and with image capture every 45 s). White-light enhancements were observed from 03:14:15 UT. Center right: difference image of the *Hinode*/SOT red continuum band at 03:15:22 UT (at an effective spatial resolution of 0.″108 pixel^{-1} and image capture every 20 s). The image captured at 03:20:06 UT was subtracted.

the Ca II H emissions were saturated, as shown in the center left and bottom left panels in Figure 2, even with their shorter exposure time. In Figure 1(c), we show the light curve for the Ca II H emission, although this is not correct for the flux after 03:15 UT because we generated this profile from observed images.

After the start of the flare mode observation, clear enhancements of the white-light emission were also observed by all three continuum filters in the SOT. For example, we show the first red difference image in the center right panel in Figure 2. We show the light curve for the red continuum emission in Figure 1(d), where the data started from 03:15:22 UT and the peak red emission was $\sim$ 1 minute earlier than the peak times of the soft X-ray, UV, and Ca II H emissions.

RHESSI also observed hard X-rays and gamma-rays at more than 1 MeV. The light curve for the hard X-ray emissions at 50–100 keV is shown in Figure 1(e). The *RHESSI* was in the SAA before 03:14:34 UT, so no hard X-ray data were available. The hard X-ray and white-light light curves are usually highly correlated (e.g., Hudson et al. 2006). However, the peak time for the hard X-ray curve appeared to be slightly earlier than that for

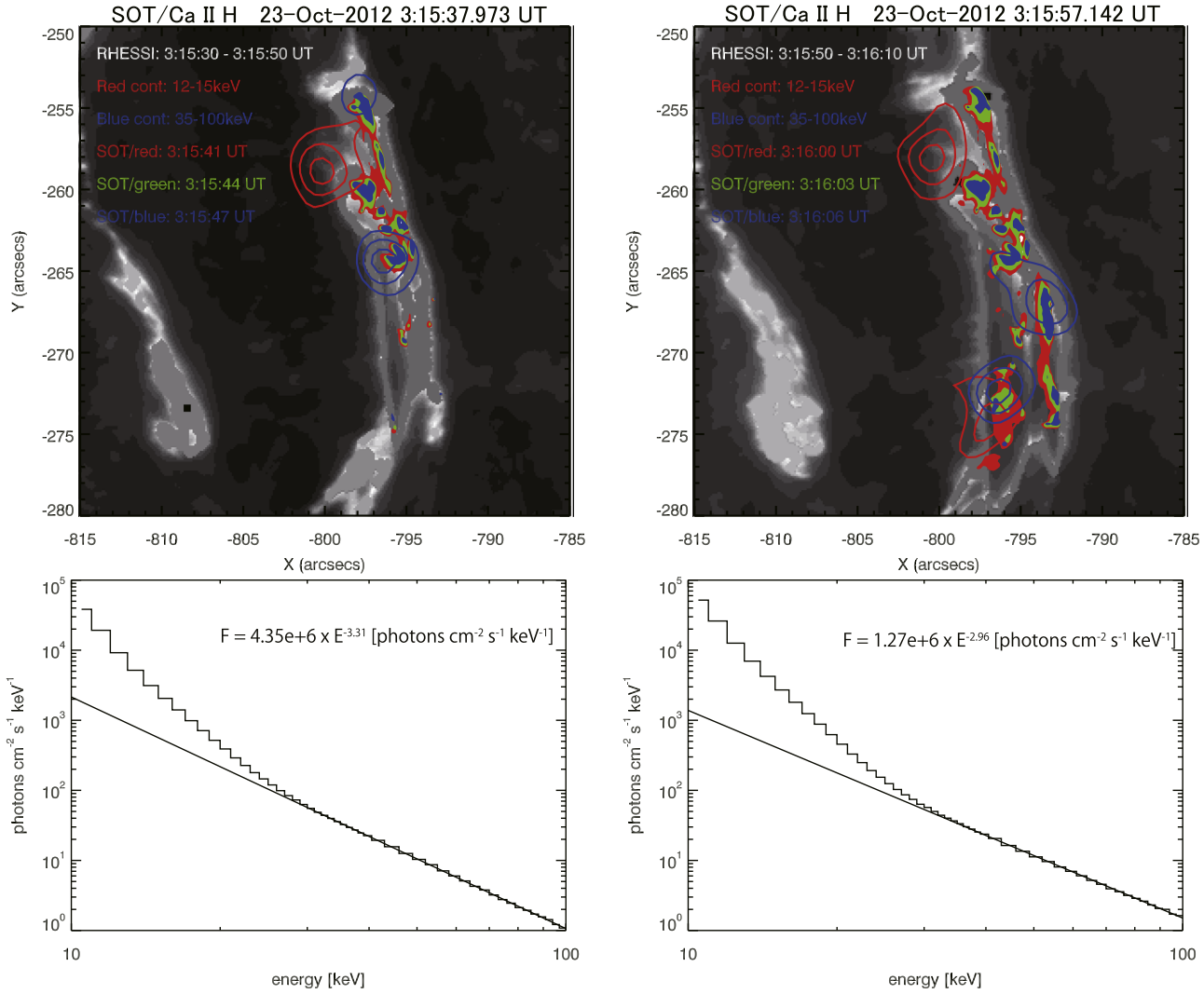

Figure 3. Top: observed Ca II H emission with white-light emission from *Hinode*/SOT and X-ray emission from *RHESSI*. The overlaying red, green, and blue filled contours indicate the deviations in intensity $\geqslant 3\sigma$ above the background for each white-light wavelength channel. White-light emission was mainly observed in the Ca II H ribbons. The overlaying red and blue contours indicate the *RHESSI* X-ray emissions with energies of 12–15 keV and 35–100 keV, respectively. Bottom: hard X-ray spectra observed by *RHESSI* at 03:15:30–03:15:50 UT (left) and 03:15:50–03:16:10 UT (right). The histograms for the observed spectra and straight lines are the fitting results obtained by using a power law for the data at 40–100 keV. The equations for these results are also shown in each figure.

the white-light curve, but the time resolution was totally different, so we cannot state this definitively.

It was difficult to determine the emission that was enhanced first due to the restricted observations and time resolution of the data. However, it is clear that the Ca II H ribbon was already formed and the hard X-ray was also emitted before the impulsive phase of the flare (~03:15 UT). At this time, no white-light data were available from the *Hinode*/SOT because this was before the flare mode observation. However, the *SDO*/HMI observed the white-light enhancement at 03:14:45 UT, as shown in the top right panel in Figure 2. Thus, the white-light emission also occurred at the beginning of the impulsive phase.

The peak time for each emission occurred slightly earlier for the hard X-ray curve than the white-light curve, as mentioned above, but this could not be differentiated clearly because of the difference in the time resolution. The peak time for the Ca II H and soft X-ray emission occurred ~1 minute later than the peak time for the red continuum emission, and the 193 Å emission peaked more than 2 minutes later than the white-light peak.

3. Observed Plasma Conditions During the Flare

The white-light emissions detected by *Hinode*/SOT were located almost exactly on the location on the strong (saturated) Ca II H ribbons and they followed their expansion, as shown in the top panels in Figure 3. The white-light emissions started to enhance from the northern part of the ribbons, before propagating to the southern part. Based on these SOT continuum data, we determined the temperature and total power of the white-light emissions by using the same methods employed by Watanabe et al. (2010a; 2013). We fitted the three color data points using the Planck formula and estimated the temperatures of the observed white-light emissions. The average temperatures in the red enhanced ($\geqslant 3\sigma$) region around 03:15:44 UT (top left panel in Figure 3) and 03:16:03 UT (top right panel in Figure 3) were estimated as 5168 K and 5170 K, respectively. Considering that the error in these temperatures is about 35 K, the same as in Watanabe et al. (2013), the temperature did not change during this period. The total power of these white-light emissions were then estimated using the Stefan–Boltzmann law as the order of 10^{28} erg s^{-1}.

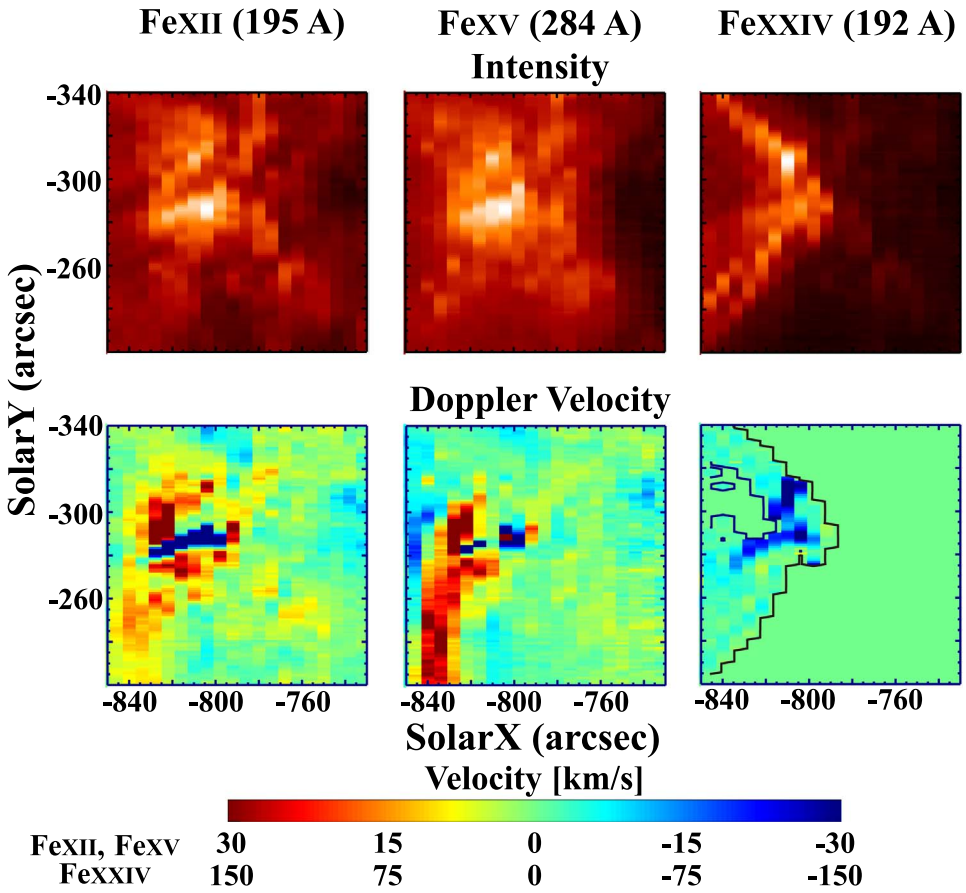

Figure 4. Intensity (top) and Doppler (bottom) maps obtained for Fe XII, Fe XV, and Fe XXIV by *Hinode*/EIS. The EIS performed a coarse raster scan (2″ slit and 5″ step) with a cadence of about 6 minutes over this active flaring region from before the flare and it appears that the flare occurred during the scan at 03:14:36 UT when the diffraction pattern in the Fe XXIV image started. The color scales for the EIS velocity maps of Fe XII and Fe XV are ±30 km s^{-1}, and ±150 km s^{-1} for Fe XXIV. These velocity maps show the strong blueshifts from the position east of the white-light ribbon, and the Fe XII and Fe XV maps show the redshifts west of the white-light ribbon.

Similar morphological features were also identified in the hard X-ray emission. In order to conduct comparisons with the white-light emission detected by *Hinode*/SOT, which was a highly compact event where the ribbons were separated by less than 5″, we prepared *RHESSI* hard X-ray images using collimators 1–3 to obtain high-resolution images. The observed hard X-ray emissions were located almost on the white-light kernels, as shown in the top panels in Figure 3, and they followed the main emission of the white-light kernels, especially at high energies. These observations indicate that nonthermal electrons existed on the white-light kernels and they might have been a source of the white-light emission.

According to these *RHESSI* data, we estimated the total power of the accelerated electrons using the method employed by Watanabe et al. (2010a). We obtained hard X-ray spectra at 03:15:30–03:15:50 UT and 03:15:50–03:16:10 UT, as shown in the bottom panels in Figure 3. We only used healthy detectors (except detectors 2 and 4) for these spectra. We fitted the 40–100 keV data with a power law and obtained equations of $F = (4.35 \pm 0.19)e + 6 \times E^{-3.31\pm0.01}$ photons cm^{-2} s^{-1} keV^{-1} and $F = (1.27 \pm 0.07)e + 6 \times E^{-2.96\pm0.01}$ photons cm^{-2} s^{-1} keV^{-1} for the two sets of spectra, respectively. When we used 40 keV as the lower energy cutoff same as Watanabe et al. (2010a), the total power of the accelerated electrons were $(1.60 \pm 0.13) \times 10^{28}$ erg s^{-1} and $(1.40 \pm 0.13) \times 10^{28}$ erg s^{-1} for the two sets of spectra, respectively. These results demonstrate that the accelerated particles with energies over 40 keV can be covered the total power of the white-light emission.

The *Hinode*/Extreme Ultraviolet Imaging Spectrometer (EIS) also successfully observed this X-class flare. The EIS is a high spectral resolution spectrometer for studying dynamical phenomena in the corona at high spatial resolution and sensitivity (Culhane et al. 2007). The flare observations were obtained by flare analysis (HH_Flare+AR_180 × 152). The EIS performed a coarse raster scan (2″ slit and 5″ step: sparse raster) with a cadence of about 6 minutes over this flaring active region from before the flare. The flare occurred during the scan. The EIS data obtained from the raster scan were processed using the EIS team software (*eis_prep*), which corrected for the flat field, dark current, cosmic rays, and hot pixels. The slit tilt was corrected by (*eis_tilt*) correction. For thermal reasons, an orbital variation in the line position causes an artificial Doppler shift of ±20 km s^{-1}, which follows a sinusoidal behavior. This orbital variation of the line position was corrected using housekeeping data (Kamio et al. 2010).

Figure 4 show the intensity and Doppler maps for Fe XII ($\log T = 6.1$), Fe XV ($\log T = 6.3$), and Fe XXIV ($\log T = 7.2$). The raster scan started from 03:11:15 UT and it required almost 6 minutes. The flare occurred during the scan at almost the center of the EIS's FOV. There were blueshifts of a few tens of km s^{-1} in the center of the Doppler map for Fe XII and Fe XV. These blueshifts were associated with the ejection during the flare,

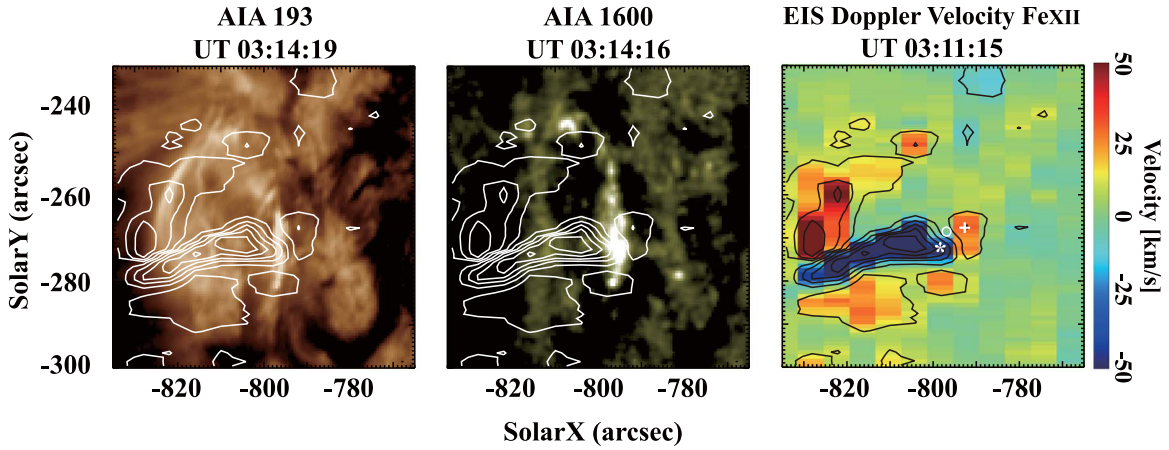

Figure 5. Intensity maps obtained for 193 (left) and 1600 Å (center) by the *SDO*/AIA, and the EIS Doppler velocity map for Fe XII (right). The overlaid contours on the AIA images indicate the same EIS Doppler velocity shown in the right panel. The region with redshifts was present west of the white-light ribbon and the blueshifts started from east of the white-light ribbon.

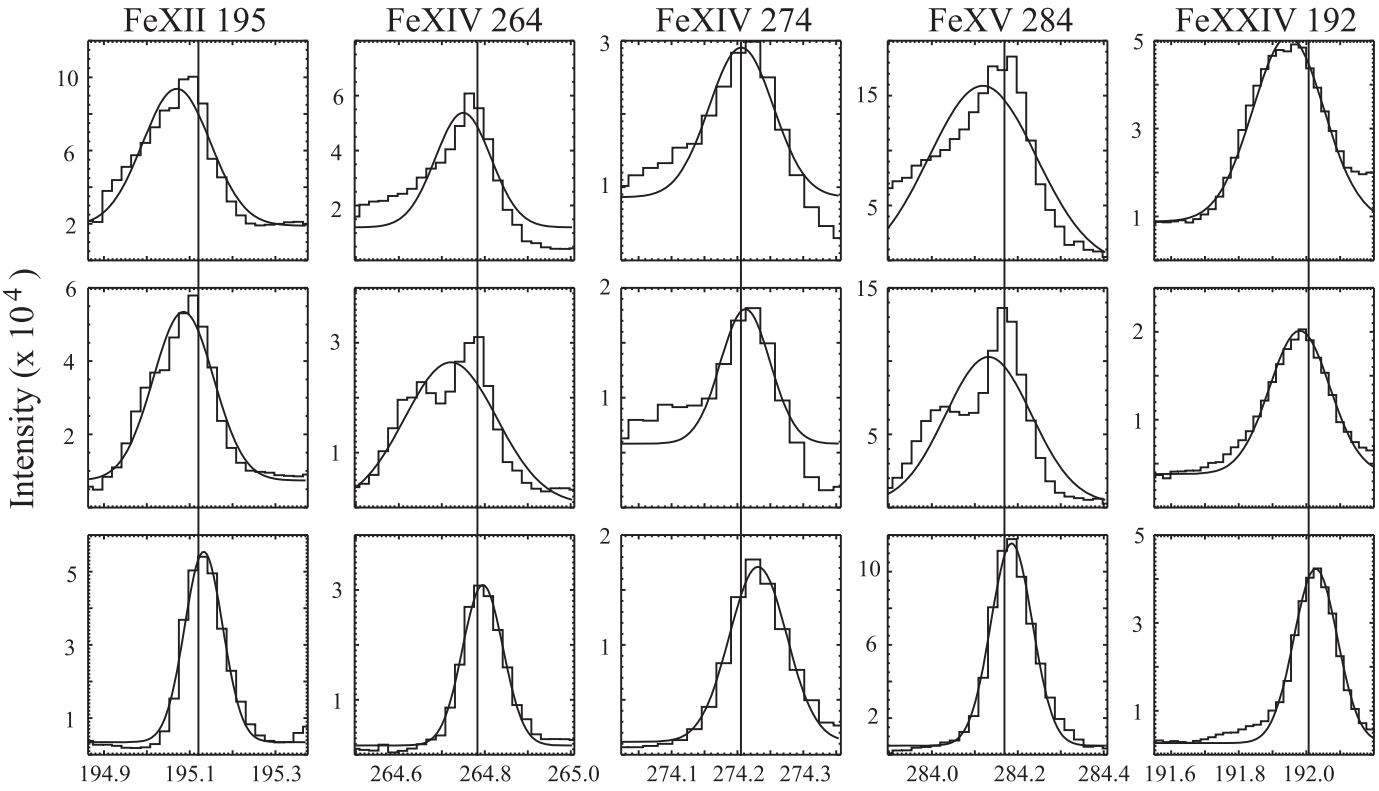

Figure 6. Samples of spectra from Fe XII, Fe XIV (264 and 274 Å), Fe XV, and Fe XXIV. The vertical axes show the intensity and the horizontal axes show the wavelength (Å). The vertical lines show the line centers of the emission lines, which were emitted from stationary ions. The upper panels show the spectra for the strong blueshift region (east ribbon; shown by the white asterisk in the right panel in Figure 5), and the lower panels show the spectra with a strong redshift region (west ribbon; shown by the white cross in the right panel in Figure 5). The middle panels show the spectra between the blueshift and redshift regions (white circle in the right panel in Figure 5).

which was clearly observed in the AIA movies. The diffraction pattern was observed in the Fe XXIV image, where the start of this pattern might have been the initial time of the impulsive phase of the flare at 03:14:36 UT. By chance, this slit position was located on one of the Ca II H ribbons that was beginning to form. According to the Fe XII data, redshifts of a few tens of km s^{-1} were observed at this time and location.

The right panel in Figure 5 is the zoomed Doppler image for Fe XII in Figure 4, and it is compared with the AIA 193 and 1600 Å images in the left and center panels, respectively. These AIA images were captured immediately after the start of the flare but ribbon-shaped enhancements were already visible, and it appears that these ribbons were located in the same position as the Ca II H ribbons and white-light enhancements, but we could not resolve two ribbons due to their resolutions. When we compared these images with SOT white-light ribbons, we can determine the redshifts were located on the west ribbon and the blueshifts started from the east ribbon.

Figure 6 shows samples of the spectra from Fe XII, Fe XIV (264 and 274 Å), Fe XV, and Fe XXIV for three positions. The

Table 1
Electron Density Variations at Three Positions

Observation Time	@ East Kernel (cm^{-3})	Between (cm^{-3})	@ West Kernel (cm^{-3})
03:10 UT (Before the flare started)	$10^{9.8}$	$10^{9.8}$	$10^{9.8}$
03:15 UT (Start of flaring)	$10^{10.4}$	$10^{10.3}$	$10^{10.2}$
03:20 UT (Flaring)	$10^{10.2}$	$>10^{12}$	$10^{11.2}$

upper panels show the spectra for the strong blueshift region (east ribbon; shown by the white asterisk in the right panel in Figure 5), the lower panels show spectra with a strong redshift region (west ribbon; shown by the white cross in the right panel in Figure 5), and the middle panels show the spectra between two ribbons (white circle in the right panel in Figure 5). In the upper panels, tails due to strong blueshifts were seen for all of the Fe lines. In the lower panels, all of the Fe lines exhibited a low number of 10 km s^{-1} downflows. These low numbers of 10 km s^{-1} downflows were also reported in previous studies (Watanabe et al. 2010b; Imada et al. 2015).

To determine the physical condition of the solar atmosphere during the white-light flare, we attempted to calculate the coronal density above the white-light kernel based on the line ratio between Fe XIV 264.79 and 274.20 Å (Young et al. 2007). We applied this method to the line spectrum shown in Figure 6 and found that the densities above the east, center, and west of the white-light kernel were $10^{10.4}$, $10^{10.3}$, and $10^{10.2}$ cm^{-3}, respectively, where the observed times for each exposure are 03:15:02, 03:14:51, and 03:14:41 UT from top to bottom in Figure 6. Furthermore, we investigated the temporal variations in the densities. For the EIS scan data starting from 03:06:05 UT, which was before the start of the flare, the profiles were fitted by single Gaussians and the density was about $10^{9.8}$ cm^{-3} in all three positions. The next scan period starting from 03:16:35 UT, which was almost the flare peak time and the profiles obtained comprised single Gaussians, was where the densities increased to $10^{10.2}$, $>10^{12}$, and $10^{11.2}$ cm^{-3} in the three positions, respectively. These results are compiled in Table 1. It seems that the white-light enhancement was only observed where the densities were less than 10^{12} cm^{-3}. Thus, it is possible that the white-light enhancement could only be observed where the plasma densities were kept lower than 10^{12} cm^{-3}.

4. Discussion and Summary

White-light emission was clearly observed by *Hinode*/SOT in association with an X1.8-class flare on 2012 October 23, and Ca II H ribbons and hard X-ray emission were also observed by *RHESSI* at almost the same location and time. *Hinode*/EIS also observed this flaring region during the flare, and redshifts of a few tens of km s^{-1} were observed for the white-light emission from before the main phase of the flare, which appear to have been related to some injection of accelerated electrons —this was the source of the white-light emission.

During this event, white-light enhancements were seen from the first image captured at 03:15:22 UT by the flare observation mode of the SOT and they were located on the saturated Ca II H ribbons. The *SDO*/HMI also observed white-light enhancements from 03:14:45 UT. It appears that chromospheric evaporation had already occurred at this time, even though the light curve had not yet peaked. Thus, most of the plasmas in the chromosphere may have already moved to the corona and the density of the chromosphere was reduced during the white-light emission.

Nonthermal electrons with energies of around 30–100 keV stop at the upper chromosphere where the electron density is $10^{13.5}$ cm^{-3} (Neidig 1989). However, if the electron density is less than $10^{13.5}$ cm^{-3}, it is possible that nonthermal electrons could reach the photosphere.

To confirm this possibility, we checked the energy range of the accelerated electrons that affected the white-light emissions and the density of the lower atmosphere. The energy range of the accelerated electrons that comprised the source of the white-light emissions was estimated as $\geqslant$40 keV, based on three continuum data sets obtained by the SOT and *RHESSI* spectra. In order to assess the density of the lower atmosphere, we determined the density of the electrons around the Fe XIV ions by using two lines from Fe XIV (264 and 274 Å). Based on the EIS scan data, we found that the electron densities of the white-light kernels were less than 10^{12} cm^{-3}, which was lower than that of the non-white-light kernel regions.

At the time of the first white-light observation in this event, electron densities were low enough (10^{10} cm^{-3}) that accelerated electrons could penetrate to the lower chromosphere. This low-density situation may be due to chromospheric evaporation, since Ca II H ribbons were already observed before the first white-light observation. Accelerated electrons must reach the chromosphere before chromospheric evaporation, however there may not have been enough that did so to produce white-light enhancement. Almost the same low densities were observed at the start time of the flare even in the non-white-light kernel regions, and it is possible that accelerated electrons also penetrated to this region. However, since higher electron densities were observed in this region during the flaring, it is considered that this region was the one where chromospheric evaporation plasma was accumulated. To summarize the above, the white-light kernel region may be a region with a low enough density to allow the accelerated electrons to penetrate, and although evaporated plasmas might not be located in the same flux tube of electron injection, the white-light kernel region may be a region where the evaporated plasma does not accumulate.

Not all solar flares exhibit white-light enhancement, even if they do exhibit evidence of electron acceleration (existence of hard X-ray emissions). Thus, some flare events exhibit white-light enhancement whereas others do not. If these are not cases where the instruments do not have enough sensitivity and time resolution, or they do not produce a significant signal above the fluctuation, two possible explanations may account for this difference: the total amount of the injected high-energy electrons could be different, or the physical condition of the chromosphere/transition region may be different.

Many previous observations indicate that there is a strong correlation between the intensity of white-light emissions and hard X-rays (e.g., Watanabe et al. 2010a; Kuhar et al. 2016).

Watanabe et al. (2017) have discussed the existence of white-light emissions based on differences in the total amount of injected high-energy electrons. However, high fluctuations can be seen in the data, which may be explained by other parameters also affecting the white-light enhancements.

Some observations and models provide insights into the physical condition of the chromosphere/transition region during solar flares. The chromospheric evaporation model (e.g., Liu et al. 2009) suggests that the chromosphere is tentatively pushed toward the photosphere and it becomes increasingly thinner and more tenuous during the impulsive phase. In addition, many observational studies (e.g., Milligan et al. 2006a, 2006b) have reported a strong correlation between the flux of incident electrons and chromospheric evaporation. Recently, redshifts in plasma of a few MK were reported during the impulsive phase (e.g., Milligan & Dennis 2009; Watanabe et al. 2010b; Li & Ding 2011; Young et al. 2013). Moreover, Imada et al. (2015) discussed the physical mechanism responsible for the strong downflows in Fe XII and Fe XV during the impulsive phase of a flare, where they performed two different numerical simulations to reproduce the strong downflows in Fe XII and Fe XV during the impulsive phase. By changing the thermal conduction coefficient, they conducted numerical calculations of the chromospheric evaporation in the thermal conduction dominant regime (conductivity coefficient κ_0 = classical value) and the enthalpy flux dominant regime ($\kappa_0 = 0.1\times$ classical value). After comparing the numerical simulations and observations, they concluded that the strong redshift could only be reproduced in the case of the enthalpy dominant regime, which corresponded to the suppression of thermal conduction and energetic electron precipitation to the chromosphere.

Hinode is a Japanese mission developed and launched by ISAS/JAXA, collaborating with NAOJ as a domestic partner, NASA and STFC (UK) as international partners. Scientific operation of the *Hinode* mission is conducted by the *Hinode* science team organized at ISAS/JAXA. This team mainly consists of scientists from institutes in the partner countries. Support for the post-launch operation is provided by JAXA and NAOJ (Japan), STFC (UK), NASA, ESA, and NSC (Norway). *RHESSI* is a NASA Small Explorer mission and we thank the *RHESSI* team for their support with the mission and guidance in the analysis of the *RHESSI* satellite data. We also thank Säm Krucker for helpful discussions regarding the *RHESSI* observations. Part of this work was conducted by the joint research program of the Institute for Space-Earth Environmental Research (ISEE), Nagoya University. This study was supported by JSPS KAKENHI grant Nos. JP15K17622, JP16H01187, JP17K14401, JP15H05816, and JP18H04452. We also appreciate fruitful comments from the anonymous referee.

ORCID iDs

Shinsuke Imada https://orcid.org/0000-0001-7891-3916

References

Battaglia, M., & Kontar, E. P. 2012, ApJ, 760, 142
Blandford, L., & Ostriker, J. P. 1978, ApJL, 221, L29
Culhane, J. L., Harra, L. K., James, A. M., et al. 2007, SoPh, 243, 19
Golub, L., DeLuca, E., Austin, G., et al. 2007, SoPh, 243, 63
Hudson, H. S., Acton, L. W., Hirayama, T., & Uchida, Y. 1992, PASJ, 44, L77
Hudson, H. S., Wolfson, C. J., & Metcalf, T. R. 2006, SoPh, 234, 79
Ichimoto, K., Lites, B., Elmore, D., et al. 2008, SoPh, 249, 233
Imada, S., Aoki, K., Hara, H., et al. 2013, ApJL, 776, L11
Imada, S., Hirai, M., Hoshino, M., & Mukai, T. 2011, JGR, 116, A08217
Imada, S., Murakami, I., & Watanabe, T. 2015, PhPl, 22, 101206
Imada, S., Nakamura, R., Daly, P. W., et al. 2007, JGR, 112, A03202
Kamio, S., Hara, H., Watanabe, T., Fredvik, T., & Hansteen, V. H. 2010, SoPh, 266, 209
Kano, R., Sakao, T., Hara, H., et al. 2008, SoPh, 249, 263
Krucker, S., Hudson, H. S., Jeffrey, N. L. S., et al. 2011, ApJ, 739, 96
Kuhar, M., Krucker, S., Martínez Oliveros, J.-C., Battaglia, M., & Kleint, L. 2016, ApJ, 816, 6
Lemen, J. R., Title, A. M., Akin, D. J., et al. 2012, SoPh, 275, 17
Li, Y., & Ding, M. D. 2011, ApJ, 727, 98
Lin, R. P., Dennis, B. R., Hurford, G. J., et al. 2002, SoPh, 210, 3
Liu, W., Petrosian, V., & Mariska, J. T. 2009, ApJ, 702, 1553
Martínez Oliveros, J.-C., Hudson, H. S., Hurford, G. J., et al. 2012, ApJL, 753, L26
Masuda, S., Kosugi, T., Hara, H., Tsuneta, S., & Ogawara, Y. 1994, Natur, 371, 495
Milligan, R. O., & Dennis, B. R. 2009, ApJ, 699, 968
Milligan, R. O., Gallagher, P. T., Mathioudakis, M., et al. 2006a, ApJL, 638, L117
Milligan, R. O., Gallagher, P. T., Mathioudakis, M., & Keenan, F. P. 2006b, ApJL, 642, L169
Neidig, D. F. 1989, SoPh, 121, 261
Øieroset, M., Lin, R. P., Phan, T. D., Larson, D. E., & Bale, S. D. 2002, PhRvL, 89, 195001
Pesnell, W. D., Thompson, B. J., & Chamberlin, P. C. 2012, SoPh, 275, 3
Sarris, E. T., Krimigis, S. M., Bostrom, C. O., Iijima, T., & Armstrong, T. P. 1976, GeoRL, 3, 437
Scherrer, P. H., Schou, J., Bush, R. I., et al. 2012, SoPh, 275, 207
Schou, J., Scherrer, P. H., Bush, R. I., et al. 2012, SoPh, 275, 229
Shimizu, T., Katsukawa, Y., Matsuzaki, K., et al. 2007, PASJ, 59, S845
Shimizu, T., Nagata, S., Tsuneta, S., et al. 2008, SoPh, 249, 221
Suematsu, Y., Tsuneta, S., Ichimoto, K., et al. 2008, SoPh, 249, 197
Tsuneta, S., Hara, H, Shimizu, T, et al. 1992, PASJ, 44, 63
Tsuneta, S., Suematsu, Y., Ichimoto, K., et al. 2008, SoPh, 249, 167
Vernazza, J. E., Avrett, E. H., & Loeser, R. 1981, ApJS, 45, 635
Watanabe, K., Kitagawa, J., & Masuda, S. 2017, ApJ, 850, 204
Watanabe, K., Krucker, S., Hudson, H., et al. 2010a, ApJ, 715, 651
Watanabe, K., Masuda, S., & Segawa, T. 2012, SoPh, 279, 317
Watanabe, K., Shimizu, T., Masuda, S., et al. 2013, ApJ, 776, 123
Watanabe, T., Hara, H., Sterling, A. C., & Harra, L. K. 2010b, ApJ, 719, 213
Young, P. R., Del Zanna, G., Mason, H. E., et al. 2007, PASJ, 59, S857
Young, P. R., Doschek, G. A., Warren, H. P., & Hara, H. 2013, ApJ, 766, 127